

This is an Open Access document downloaded from ORCA, Cardiff University's institutional repository:<https://orca.cardiff.ac.uk/id/eprint/174330/>

This is the author's version of a work that was submitted to / accepted for publication.

Citation for final published version:

Oberhauser, Werner, Evangelisti, Claudio, Nguyen, Xuan Trung, Filippi, Jonathan, Poggini, Lorenzo, Capozzoli, Laura, Manca, Gabriele, Kitching, Ella A., Slater, Thomas J. A. and Danaie, Mohsen 2024. Effect of Pt nanoparticle morphology on the aerobic oxidation of ethylene glycol to glycolic acid in water. *Inorganic Chemistry* 63 (48) , pp. 22912-22922. 10.1021/acs.inorgchem.4c03970

Publishers page: <https://doi.org/10.1021/acs.inorgchem.4c03970>

Please note:

Changes made as a result of publishing processes such as copy-editing, formatting and page numbers may not be reflected in this version. For the definitive version of this publication, please refer to the published source. You are advised to consult the publisher's version if you wish to cite this paper.

This version is being made available in accordance with publisher policies. See <http://orca.cf.ac.uk/policies.html> for usage policies. Copyright and moral rights for publications made available in ORCA are retained by the copyright holders.



# **Effect of Pt Nanoparticle Morphology on the Aerobic Oxidation of Ethylene Glycol to Glycolic Acid in Water**

**Werner Oberhauser<sup>a\*</sup> Claudio Evangelisti<sup>b\*</sup>, Xuan Trung Nguyen<sup>b</sup>, Jonathan Filippi<sup>a</sup>, Lorenzo Poggini<sup>a,c</sup>, Laura Capozzoli<sup>a</sup>, Gabriele Manca<sup>a</sup>, Ella A. Kitching<sup>d</sup>, Thomas J. A. Slater<sup>d</sup>, and Mohsen Danaie<sup>e</sup>**

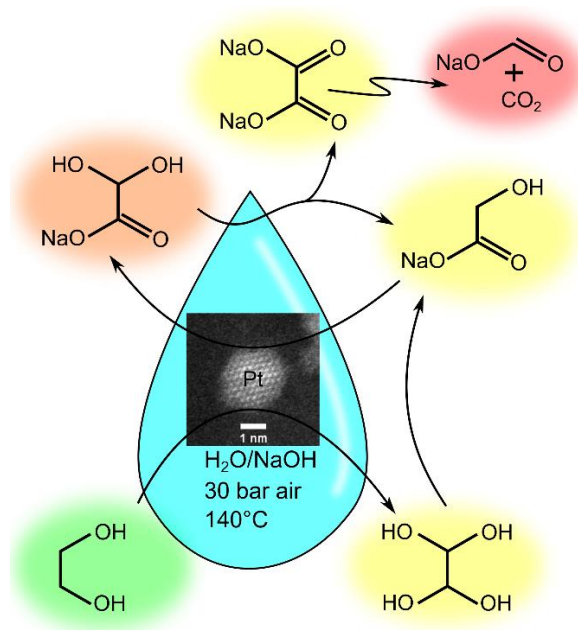
<sup>a</sup>Istituto di Chimica dei Composti Organometallici (CNR-ICCOM) Via Madonna del Piano 10, 50019 Sesto Fiorentino, Italy; E-mail: [werner.oberhauser@iccom.cnr.it](mailto:werner.oberhauser@iccom.cnr.it)

<sup>b</sup>Istituto di Chimica dei Composti Organometallici (CNR-ICCOM) UOS Pisa, Via G. Moruzzi 1, 56124 Pisa, Italy; E-mail: [claudio.evangelisti@cnr.it](mailto:claudio.evangelisti@cnr.it)

<sup>c</sup>Department of Chemistry “U. Schiff”-DICUS and INSTM Research Unit, University of Florence, Via della Lastruccia 3-13,50019 Sesto Fiorentino, Italy

<sup>d</sup>Cardiff Catalysis Institute (CCI), Cardiff University, Maindy Road, Cardiff CF24 4HQ, United Kingdom

<sup>e</sup>electron Physical Science Imaging Centre (ePSIC), Diamond Light Source, Harwell Science & Innovation Campus, Didcot, Oxfordshire OX11 0DE, United Kingdom



**ABSTRACT:** Pt nanoparticles (diameter < 3 nm), generated by metal vapor synthesis and supported on a high surface area carbon were used to catalyze the aerobic oxidation of ethylene glycol to glycolic acid (GA) in water under neutral and basic reaction conditions. Controlled heat-treatment of the catalyst under a nitrogen atmosphere brought about the formation of a morphologically well-defined catalyst. A combination of atomic-resolution electron microscopy, CO-stripping voltammetry and XPS analyses conducted on as-synthesized and heat-treated catalysts demonstrated the crucial role of the nanoparticles' morphology on the stabilization of catalytically highly active Pt-OH surface species, which were key species for the Pt-catalyzed oxidation of the alcohol to the carbonyl functionality. The boosting effect of base on the catalyst' s activity and GA selectivity has been proved experimentally (autoclave experiments). The effect of base on the non-metal catalyzed reaction steps (*i.e.* aerobic oxidation of carbonyl to acid functionality) has been proved by DFT calculations.

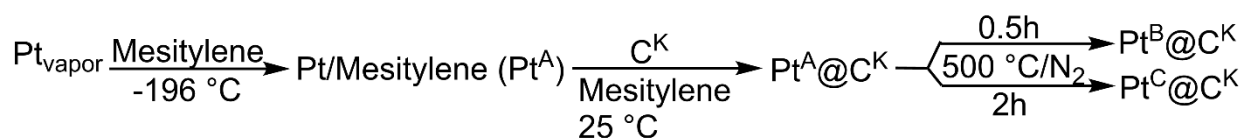
## INTRODUCTION

Glycolic acid (GA), which is the simplest hydroxy acid and generally obtained through metabolic synthesis routes by the vast majority of living organisms,<sup>1</sup> is used as a cleaning agent, for metal

chelation, for the production of cosmetics (skincare) and the production of polyesters such as polyglycolide and poly-(lactide-*co*-glycolide),<sup>2,3</sup> which are suitable candidates for biomedical application and tissue engineering.<sup>4,5</sup> Known commercial routes to synthesize GA are: (i) the hydrolysis of methyl glycolate or glyconitrile (*i.e.* obtained from HCN and formaldehyde),<sup>6</sup> (ii) the hydrolysis of chloracetic acid<sup>7</sup> and (iii) the carbonylation of formaldehyde and derivatives thereof such as dimethoxy methane, dioxolane, trioxymethylene, polyoxymethylene and para-formaldehyde,<sup>8</sup> followed by hydrolysis of the obtained poly (glycolic acid).<sup>9</sup> All these latter synthesis routes are based on fossil fuel feedstocks and should hence be replaced by biomass-based ones<sup>10</sup> such as cellulose,<sup>11-15</sup> sugars,<sup>11-13</sup> polyols,<sup>15-21</sup> glyoxal (GLY),<sup>22</sup> and oxalic acid (OA).<sup>23</sup> From an economic and environmental point of view, aerobic ethylene glycol (EG) oxidation to GA is the most favourable synthesis pathway.<sup>15</sup> This is particularly interesting, since many efficient synthesis pathways for EG have been reported so far, using cellulose as the starting material.<sup>24-29</sup> Apart from heterogeneous Pd-<sup>16,17</sup> and Au-,<sup>17,30</sup> based catalysts, Pt-nanoparticle (NP)-based catalysts<sup>18,19,21</sup> and even a platinum atom-based catalyst, which revealed high catalytic activity along with a low metal leaching compared to NP-based catalysts,<sup>31</sup> have been mostly employed in the aerobic oxidation of EG to GA in water. Alloyed Pt NPs have been shown to increase GA selectivity in aerobic EG oxidation reactions conducted under basic reaction condition.<sup>21</sup> On the other hand, the effect of structural and morphological features of Pt NPs' on GA selectivity has not yet been elucidated. It is known that upon controlled heating of NPs in a given atmosphere (*i.e.* H<sub>2</sub>, CO, O<sub>2</sub>)<sup>32-35</sup> surface atoms experience a re-arrangement that results in new structures that are more thermodynamically favourable.<sup>36-40</sup> In addition, the morphology of the Pt-NPs (*i.e.* exposed facets) is important for the successful oxygen activation in water to generate the catalytically active surface Pt(II)-OH species.<sup>41</sup> Herein, we show that the Pt NP morphology in combination with basic reaction condition steer the catalysts' activity along with the GA selectivity in the aerobic oxidation of EG in water.

## RESULTS AND DISCUSSION

**Catalysts' synthesis and characterization.** Ultrasmall Pt NPs were synthesized by metal vapor synthesis (MVS)<sup>42</sup> and the obtained mesitylene-stabilized NPs (Pt<sup>A</sup>) were then supported onto Ketjenblack (C<sup>K</sup>, high surface area carbon, characterized by a high surface area of 1490 m<sup>2</sup>/g) giving Pt<sup>A</sup>@C<sup>K</sup> (Scheme 1). A fraction of Pt<sup>A</sup>@C<sup>K</sup> was then heat-treated in a nitrogen atmosphere at 500 °C (*i.e.* temperature at which Pt atoms on the NPs surface exhibit a notable mobility in a rational time)<sup>35</sup> for half an hour and two hours giving Pt<sup>B</sup>@C<sup>K</sup> and Pt<sup>C</sup>@C<sup>K</sup>, respectively (Scheme 1). The Pt loading in Pt<sup>A</sup>@C<sup>K</sup> was of 1.2 wt% (Inductively coupled plasma optical emission spectroscopy, ICP-OES, analysis).



**Scheme 1.** Syntheses of Pt<sup>A/B/C</sup>@C<sup>K</sup> by MVS approach.

All three carbon-supported Pt samples have been analyzed by High-angle annular dark-field scanning transmission electron microscopy (HAADF-STEM), CO-stripping voltammetry and X-ray photoelectron spectroscopy (XPS) and the most relevant analytical data are compiled in Table 1.

**Table 1. Catalysts' characterization by STEM, XPS and electrochemical CO stripping voltammetry**

Catalyst	HAADF-STEM	XPS	Electrochemical CO stripping
	ECD <sub>m</sub> (nm) /Pt dispersion (%)	B.E. (eV) of Pt 4f <sub>7/2</sub> (atom % for Pt(0), Pt(2+) and Pt(4+))	E <sub>onset</sub> /E <sub>peak</sub> (V) (RHE)/ECSA (m <sup>2</sup> /g)
Pt <sup>A</sup> @C <sup>K</sup>	0.9 ± 0.3/73	71.9 (80.2)/73.5 (6.6) 75.4 (13.2)	0.815/0.908 (201.4)
Pt <sup>B</sup> @C <sup>K</sup>	1.5 ± 0.5/50	71.8 (77.4)/73.5 (5.0) 75.1 (17.6)	0.839/0.915 (105.6)
Pt <sup>C</sup> @C <sup>K</sup>	1.4 ± 0.5/n.d.	71.7 (78.7)/73.5 (7.2) 75.4 (14.1)	0.845/0.960 (124.6)

HAADF imaging in the aberration-corrected STEM was undertaken to calculate particle size distributions (PSD) and to determine the proportion of single atoms post heat-treatment. The samples showed a clear decrease in the proportion of single atoms and an increase in diameter after heat treatment (Figure 1). Imaging of Pt<sup>A</sup>@C<sup>K</sup> uncovered a high proportion of single atoms, and the presence of 1-2 nm NPs (mean diameter of 0.9 nm, single atoms excluded from calculation) (Figure 1). Heat-treatment for 30 minutes (Pt<sup>B</sup>@C<sup>K</sup>) resulted in all NPs having a sub-3 nm diameter (mean diameter of 1.5 nm), and heat-treatment for 2 hours (Pt<sup>C</sup>@C<sup>K</sup>) resulted in 82% of NPs having a sub-3 nm diameter (mean diameter of 1.4 nm), along with NPs of larger size (ranging from 10-50 nm in diameter, with an overall sample mean diameter of 3.3 nm and a standard deviation of 7.4 nm).

Analysis of number of single atoms in comparison to approximate volume of NPs demonstrated that approximately 6% of all total atoms observed in Pt<sup>A</sup>@C<sup>K</sup> were single atoms, whereas in Pt<sup>B</sup>@C<sup>K</sup> and Pt<sup>C</sup>@C<sup>K</sup> this portion is negligible (*i.e.* reduced to 0.1% and 0%, respectively).

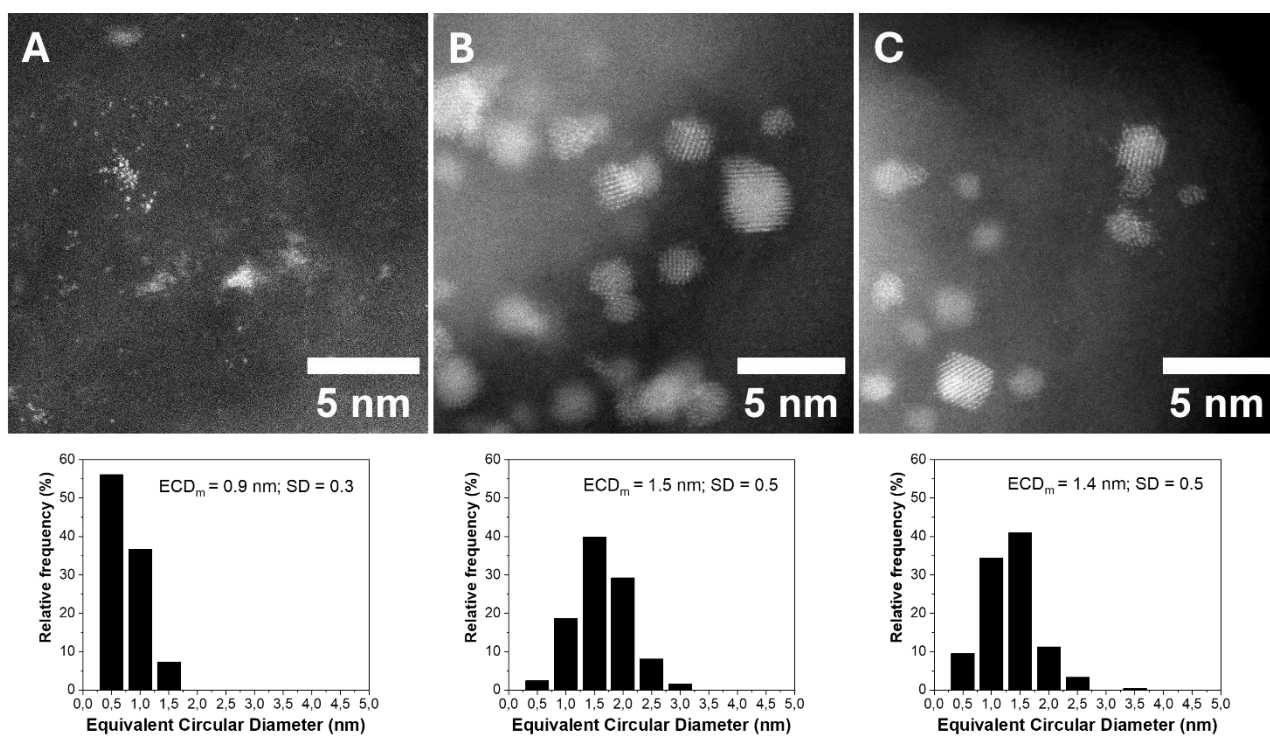


**Figure 1.** HAADF-STEM images and related particle size distributions within 0.3 – 3.0 nm range and mean equivalent circular diameter (ECD<sub>m</sub>) of: Pt<sup>A</sup>@C<sup>K</sup> (A), Pt<sup>B</sup>@C<sup>K</sup> (B) and Pt<sup>C</sup>@C<sup>K</sup> (C).

The Pt dispersion in Pt<sup>A/B</sup>@C<sup>K</sup> has been determined by estimating the total surface atoms and bulk atoms in each observed NP based on their equivalent circular diameter (Figure 1).<sup>43</sup> As a result, Pt<sup>A</sup>@C<sup>K</sup> and Pt<sup>B</sup>@C<sup>K</sup> gave a metal dispersion of 73% and 50%, respectively (Table 1). Pt<sup>C</sup>@C<sup>K</sup> had an inhomogeneous size distribution and was affected by NP aggregation, hence the estimation of the surface Pt atoms based on TEM measurements was not reliable. The NPs present in Pt<sup>B/C</sup>@C<sup>K</sup> were variable in morphology and crystallinity. There were instances of NPs in the size regime 1-2 nm which appear to be amorphous, but the majority of NPs of diameter greater than 1 nm possessed the typical *fcc* Pt structure. The majority of NPs had a single domain, but instances of twinned domains characteristic of decahedral NPs were observed (Figures 1B, S1).<sup>44</sup> Crystalline NPs displayed a mixture of low-index facets (*i.e.* {111} and {110}) in a ratio of approximately 2:1 for Pt<sup>B</sup>@C<sup>K</sup> and 3:1 for Pt<sup>C</sup>@C<sup>K</sup>) and high-index facets, commensurate with the variability of morphologies present (Figure S1).

In order to better characterize the Pt NPs' surface in Pt<sup>A/B/C</sup>@C<sup>K</sup>, CO stripping experiments, which are known to be highly surface sensitive for Pt NPs were carried out.<sup>45-47</sup> As a result, the corresponding current (J) vs oxidation potential (E) curves are shown in Figure 2. The NPs' size, shape and agglomeration notably influences the oxidation potential at which the reaction between surface adsorbed CO and OH<sup>-</sup> groups, following a Langmuir-Hinshelwood mechanism, occurs. Oxidation potentials higher than 0.88 V (RHE) are generally a strong indication for well-dispersed small-sized Pt-NPs (1.7 nm).<sup>46</sup> In accordance, we found that the onset potential for CO oxidation shifted to higher values by heat-treating of Pt<sup>A</sup>@C<sup>K</sup> (Table 1) (*i.e.* the latter sample has the lowest  $E_{\text{onset}}$  of 0.815 V, due to the presence of the smallest Pt NPs, Pt clusters and atoms (TEM analysis)). In addition, heat treatment of Pt<sup>A</sup>@C<sup>K</sup> had also a consequence on the electrochemical surface area (ECSA) given in m<sup>2</sup> g<sup>-1</sup> observed (Table 1). This notable decrease of ECSA obtained for Pt<sup>B</sup>@C<sup>K</sup> compared to Pt<sup>A</sup>@C<sup>K</sup> is due to the presence of well-shaped NPs in Pt<sup>B</sup>@C<sup>K</sup> characterized by a homogeneous size distribution and a larger average size of the NPs and almost absence of Pt atoms on the carbon surface, in accordance with TEM results. In contrast, Pt<sup>C</sup>@C<sup>K</sup> showed a large, ill-shaped J/E curve, which is consistent with the presence of NPs characterized by a large NP size distribution in accordance with TEM results.

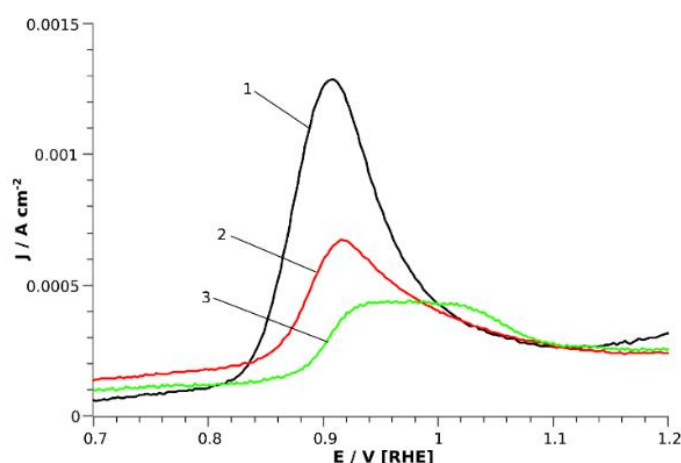


**Figure 2.** CO-stripping voltammetry with subtracted background current for Pt<sup>A</sup>@C<sup>K</sup> (1) and Pt<sup>B</sup>@C<sup>K</sup> (2) and Pt<sup>C</sup>@C<sup>K</sup> (3).

XPS analyses of  $\text{Pt}^{\text{A/B/C}}@C^{\text{K}}$  showed upon deconvolution of the Pt 4f photoelectron spectra (**Figure 3**) the presence of three distinct Pt oxidation states (*i.e.* Pt (0/2+/4+)) (*i.e.* the binding energies (B.Es.) for the Pt 4f<sub>7/2</sub> photoelectron are given in Table 1). The major fraction of surface Pt B.Es. in the range between 71.7-71.9 eV (Table 1) correspond to the metallic state of Pt,<sup>48</sup> while the Pt 4f<sub>7/2</sub> photoelectron peak centered at a B.E. of 73.5 eV was assigned to Pt (2+) (PtO).<sup>48</sup> An additional Pt 4f<sub>7/2</sub> photoelectron emission in the B.E. interval from 75.1 to 75.4 eV (Table 1) corresponded to that found for PtO<sub>2</sub>.<sup>48</sup> The atom percentage of surface oxidized Pt atoms (Pt (2+/4+)) was found to be larger in the heat-treated samples compared to the as-synthesized one (*i.e.* 22.6% (Pt<sup>B</sup>@C<sup>K</sup>), 21.3% (Pt<sup>C</sup>@C<sup>K</sup>) and 19.8% (Pt<sup>A</sup>@C<sup>K</sup>).

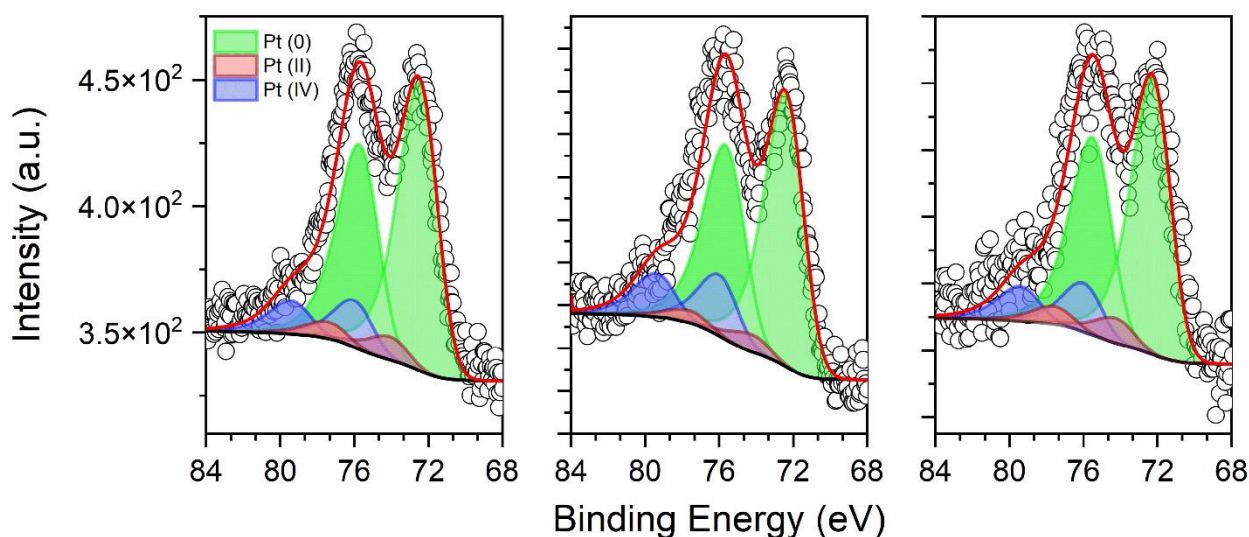
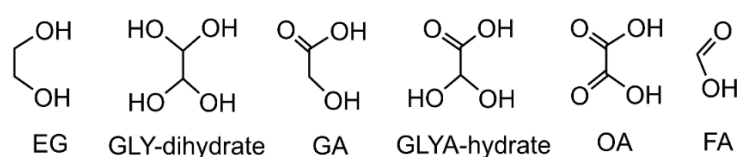


**Figure 3.** Pt 4f photoelectron spectra for Pt<sup>A</sup>@C<sup>K</sup> (left), Pt<sup>B</sup>@C<sup>K</sup> (middle) and Pt<sup>C</sup>@C<sup>K</sup> (right).

**Catalysis.**  $\text{Pt}^{\text{A/B/C}}@C^{\text{K}}$  have been used to catalyze the aerobic oxidation (air, 30 bar) of EG in water (0.274M) at 140 °C under neutral and basic reaction conditions. In order to gain reproducible EG conversions and to exclude diffusion problems due to substrate transport limitations to the catalytic sites, we carefully adjusted the stirrer speed of the autoclave (*i.e.* 1000 rpm resulted as the optimal stirrer speed). All catalytic results gathered in Table 2, are reported as average value of three independent catalytic reactions (*i.e.* an error of 1.5-2% for all catalytic runs shown in Table 2). The

water solutions were analyzed after catalysis by means of HPLC (Figures S2 and S3) (*i.e.* an error of 1.0-1.5 % was found for three consecutive analyses of the same sample) and the intercepted products were identified by using authentic samples, whereas the head space of the catalyst was analyzed by GC-TCD (Figure S4) (an error of 2.0-2.5% was registered for three consecutive analyses of the same sample). The organic products intercepted in solution are shown in Scheme 2 (*i.e.* EG, glyoxal (GLY)-dihydrate, GA, glyoxylic acid (GLYA)-hydrate, OA and formic acid (FA)).



**Scheme 2.** Organic compounds intercepted in water solution of the aerobic EG oxidation.

Pt<sup>A</sup>@C<sup>K</sup> gave under neutral reaction condition an EG conversion of 32.4% along with a GA selectivity of only 34.1% (Table 2, entry 10). Upon exchanging the air atmosphere by nitrogen (30 bar), the EG conversion dropped to 1.8% (Table 2, entry 9). This latter catalytic result clearly shows the need of oxygen to give a rational EG conversion to GA. Analogous catalytic reactions conducted under air atmosphere in the presence of Pt<sup>B/C</sup>@C<sup>K</sup> gave in either case an increased EG conversion compared to Pt<sup>A</sup>@C<sup>K</sup>, with the best GA selectivity of 40.5% shown for Pt<sup>B</sup>@C<sup>K</sup> (Table 2, entry 11), whereas Pt<sup>C</sup>@C<sup>K</sup> showed a high conversion to CO<sub>2</sub> at the expense of the GA selectivity (Table 2, entry 13 *vs* entry 11). Under neutral reaction conditions FA was found to be the major liquid side product.

We also proved the reactivity of GA in the presence of Pt<sup>B</sup>@C<sup>K</sup> (most active catalyst) under neutral aerobic reaction condition. As a result, the GA conversion was found to be significantly higher compared to that of EG under identical catalytic condition, giving almost quantitatively CO<sub>2</sub> (95.9%,

Table 2, entry 12 vs entry 11). In addition, blank reactions with EG and GA led to negligible substrate conversion (Table 2, entries 4 and 1), whereas analogous reactions with GLY dihydrate, GLYA hydrate and OA gave FA as major liquid product and CO<sub>2</sub> as the only gaseous product (Table 2). GLY dihydrate was quantitatively converted to GA (100% selectivity) under nitrogen atmosphere in the absence of a metal catalyst. Combining hence the results obtained from metal-catalyzed and blank reactions conducted under neutral reaction condition, we can infer that the conversion of EG to GLY dihydrate and of GA to GLYA hydrate are Pt-NP-catalyzed reactions and that the former conversion is slower compared to latter.

**Table 2. Aerobic oxidation reactions in water**

Neutral reaction condition <sup>a</sup>							
Entry	Cat.	Sub.	Conv. (%) / [TOF (h <sup>-1</sup> )]	GA (mmol) / Sel. (%) <sup>b</sup>	GLY/GLYA/OA/FA (mmol)	Σ Products (mmol)/(%)	CO <sub>2</sub> (mmol)/(%)
1	-	EG	1.4	n.d.	n.d.	n.d.	n.d.
2	-	GLY	100.0	5.3/38.7	-/-/4.4	9.7/70.4	4.0/29.6
3 <sup>c</sup>	-	GLY	100.0	13.7/100.0	-	13.7	-
4	-	GA	1.4	n.d.	n.d.	n.d.	n.d.
5	-	GLYA	99.7	-	-/-/2.3	2.3/16.8	11.4/83.2
6 <sup>c</sup>	-	GLYA	97.7	6.6/49.2	-/-/0.2/-	6.8/50.6	6.6/49.4
7	-	OA	100.0	-	-/-/0.7	0.7/5.4	13.0/94.6
8 <sup>c</sup>	-	OA	99.8	-	-/-/4.8	4.8/35.3	8.8/64.7
9 <sup>c</sup>	Pt <sup>A</sup> @C <sup>K</sup>	EG	1.8 [n.d.]	n.d.	n.d.	n.d.	n.d.
10	Pt <sup>A</sup> @C <sup>K</sup>	EG	32.4 [186]	1.5/34.1	-/-/0.2	1.7/39.2	2.7/60.8
11	Pt <sup>B</sup> @C <sup>K</sup>	EG	30.7 [260]	1.7/40.5	-/-/0.1	1.8/42.8	2.4/57.1
12	Pt <sup>B</sup> @C <sup>K</sup>	GA	53.3 [449]	-	-/-/0.3	0.3/4.1	7.0/95.9
13	Pt <sup>C</sup> @C <sup>K</sup>	EG	42.3 [n.d.]	1.4/24.1	0.1/-/0.2	1.7/29.3	4.1/70.7
Basic reaction condition <sup>d</sup>							
14	-	EG	5.0	n.d.	n.d.	n.d.	n.d.
15	-	GA	<1.0	n.d.	n.d.	n.d.	n.d.
16	Pt <sup>A</sup> @C <sup>K</sup>	EG	30.9 [1017]	2.8/66.7	-/-/1.4	4.2/100.0	-
17 <sup>e</sup>	Pt <sup>A</sup> @C <sup>K</sup>	EG	74.0 [914]	4.4/43.6	-/-/1.1/2.7	8.2/81.2	1.9/18.8
18 <sup>f</sup>	Pt <sup>B</sup> @C <sup>K</sup>	EG	45.7 [6590]	5.5/87.3	-/-/0.3/0.5	6.3/100.0	-
19	Pt <sup>B</sup> @C <sup>K</sup>	EG	77.4 [3721]	7.7/72.6	-/-/0.2/1.7	9.6/90.6	1.0/9.4
20 <sup>g</sup>	Pt <sup>B</sup> @C <sup>K</sup>	EG	56.0 [n.d.]	4.9/63.6	-/-/0.1/2.6	7.6/98.7	0.1/1.3
21 <sup>h</sup>	Pt <sup>B</sup> @C <sup>K</sup>	EG	92.0 [2211]	8.2/65.1	-/-/0.6/2.3	11.1/88.1	1.5/11.9
22 <sup>i</sup>	Pt <sup>B</sup> @C <sup>K</sup>	EG	84.0 [4038]	7.6/66.1	-/-/0.2/3.2	11.0/95.6	0.5/4.4
23	Pt <sup>B</sup> @C <sup>K</sup>	GA	39.3 [n.d.]	-	-/-/0.1/2.1	2.2/40.7	3.2/59.3
24 <sup>i</sup>	Pt <sup>B</sup> @C <sup>K</sup>	GA	53.0 [n.d.]	-	-/-/0.2/3.1	3.3/45.2	4.0/54.8
25	Pt <sup>C</sup> @C <sup>K</sup>	EG	50.1 [n.d.]	4.8/69.6	-/-/0.1/1.2	6.1/88.4	0.7/10.1

<sup>a</sup>Catalytic condition: Pt (1.90 μmol), T (140 °C), p(air) (30 bar) at 140 °C, substrate (13.7 mmol), t (17h); <sup>b</sup>Selectivity (GA) (%) defined as: mmol (GA) / mmol (EG conv.); <sup>c</sup>N<sub>2</sub> atmosphere (30 bar); <sup>d</sup>NaOH (13.7 mmol), t (3h); <sup>e</sup>t (8h); <sup>f</sup>t (1h); <sup>g</sup>(1<sup>st</sup> recycling); <sup>h</sup>t (6h); <sup>i</sup>NaOH (27.4 mmol).

Blank reactions conducted with EG and GA in the presence of NaOH (*i.e.* one molequivalent with respect to the substrate), exhibited only negligible substrate conversion (Table 2, entries 14 and 15). On the other hand, Pt<sup>A/B/C</sup>@C<sup>K</sup>-catalyzed reactions experienced a notable EG conversion in the presence of base. In fact, this boosting effect of on the catalytic activity exerted by the base is clearly evident by comparing the catalytic activity (*i.e.* expressed in surface-atom-related TOF) obtained for each catalyst under neutral and basic reaction conditions (Table 2). Within the series of catalysts studied herein, Pt<sup>B</sup>@C<sup>K</sup> exhibited under basic reaction condition the highest activity for EG conversion (*i.e.* Table 2, entry 19 *vs* entries 16 and 25). The reactivity of GA under basic reaction condition was found to be much lower compared to that of EG under identical reaction condition, which is the opposite trend found under neutral reaction condition with the same catalyst (*i.e.* Table 2, entry 23 *vs* entry 19 (basic reaction condition) and entry 12 *vs* entry 11 (neutral reaction condition)).

Upon increasing the amount of base (two molequivalents with respect to the amount of EG) the Pt<sup>B</sup>@C<sup>K</sup>-catalyzed EG conversion increased at the expense of the GA selectivity, due to a significant formation of sodium formate (Table 2, entry 22 *vs* entry 19).

In order to justify the reaction parameters (*i.e.* reaction temperature and air pressure) chosen for the catalytic reactions, we carried out parallel catalytic reactions with Pt<sup>B</sup>@C<sup>K</sup> under basic reaction conditions (Table 2) by changing reaction temperature and air pressure. As a result, we found at 120 °C and 30 bar air pressure an EG conversion of 59.2% with an GA selectivity of 91.0% and at 140 °C and 20 bar air pressure an EG conversion of 70.1% and a GA selectivity of 76.1%, while at 140 °C and 40 bar air pressure an EG conversion of 79.0% along with a GA selectivity of 71.0% was obtained. Hence a reaction temperature lower than 140 °C led to a significant drop of EG conversion, while an increase of the air pressure from 30 to 40 bar at 140 °C gave a result comparable to that obtained at 140 °C and an air pressure of 30 bar (Table 2, entry 19).

Recovered Pt<sup>B</sup>@C<sup>K</sup> was recycled once to test its stability under real aerobic oxidation condition. As a result, the catalytic activity and GA selectivity dropped significantly with respect to that obtained

with fresh Pt<sup>B</sup>@C<sup>K</sup> (*i.e.* GA selectivity of 63.6% at 56.0 EG conversion (recycled Pt<sup>B</sup>@C<sup>K</sup>) vs GA selectivity of 72.6% at 77.4% EG conversion (fresh Pt<sup>B</sup>@C<sup>K</sup>). In order to verify leaching of Pt into water solution during catalysis, in a parallel reaction, the autoclave was cooled to 100 °C, the gases released from autoclave, the suspension filtered at the latter temperature and the clear solution analyzed by ICP-OES. As a result, a Pt leaching of 3.4 % (*i.e.* with respect to the initial amount of Pt used) was found. Powder X-ray diffraction (PXRD) spectra acquired for Pt<sup>A</sup>@C<sup>K</sup> and Pt<sup>B</sup>@C<sup>K</sup>, recovered after catalytic reactions conducted under identical experimental condition (*i.e.* 140 °C, 3h, p(air) 30 bar, EG 13.7 mmol, NaOH, 13.7 mmol) are shown in Figure S6. As a result, the PXRD trace for Pt<sup>A</sup>@C<sup>K</sup> shows the clear presence of the Pt(111) Bragg reflex (*i.e.* due to NP aggregation), which is completely absent in the corresponding spectrum acquired for Pt<sup>B</sup>@C<sup>K</sup>. Hence this experimental result is indicative for the significantly lower stability of Pt<sup>A</sup>@C<sup>K</sup> compared to Pt<sup>B</sup>@C<sup>K</sup> against NP aggregation under real catalytic condition, which is due to the high mobility of Pt atoms and clusters present in Pt<sup>A</sup>@C<sup>K</sup>.

HRTEM analysis of the recovered catalyst showed an average particle size of 1.7 nm (Figure S5), which is only slightly larger compared to fresh Pt<sup>B</sup>@C<sup>K</sup> (*i.e.* 1.5 nm). On the other hand, XPS analysis of recovered Pt<sup>B</sup>@C<sup>K</sup> clearly showed a notable increase of the atom percentage of oxidized surface Pt-atoms (*i.e.* 51.1 % vs 22.6% (fresh catalyst) (Figure S6). In particular, the notable increase of the fraction of surface Pt(4+) during the catalytic reaction (*i.e.* 34.1% vs 17.6%, fresh catalyst) is indicative for the over-oxidation of Pt NPS which leads to the formation of a surface Pt-oxide phase which is similar to that of PtO<sub>2</sub>.<sup>49</sup>

**DFT calculations.** The GLY to GA conversion in water in the absence of a metal-catalyst was studied by DFT calculations and NMR spectroscopy. GLY dihydrate connected to four water molecules (**1**) has been chosen as starting model compound for GLY in water (Figure S7). The intramolecular 1,2-hydride shift of **1**<sup>50</sup> under neutral reaction condition did not lead to the formation of GA, instead

*ortho*-GA coordinated to water molecules (**2**) was obtained (Figure S7) and the corresponding transition state (TS<sub>1-2</sub>) was found to be of 89.8 kcal mol<sup>-1</sup> (Figure 4). The dehydration of **2** was associated with a Free Energy cost of 29.1 kcal mol<sup>-1</sup> (TS<sub>2-3</sub>, Fig. 4). GA (**3**) is energetically favoured over *ortho*-GA (**2**) by 20.3 kcal mol<sup>-1</sup> (Figure 4).

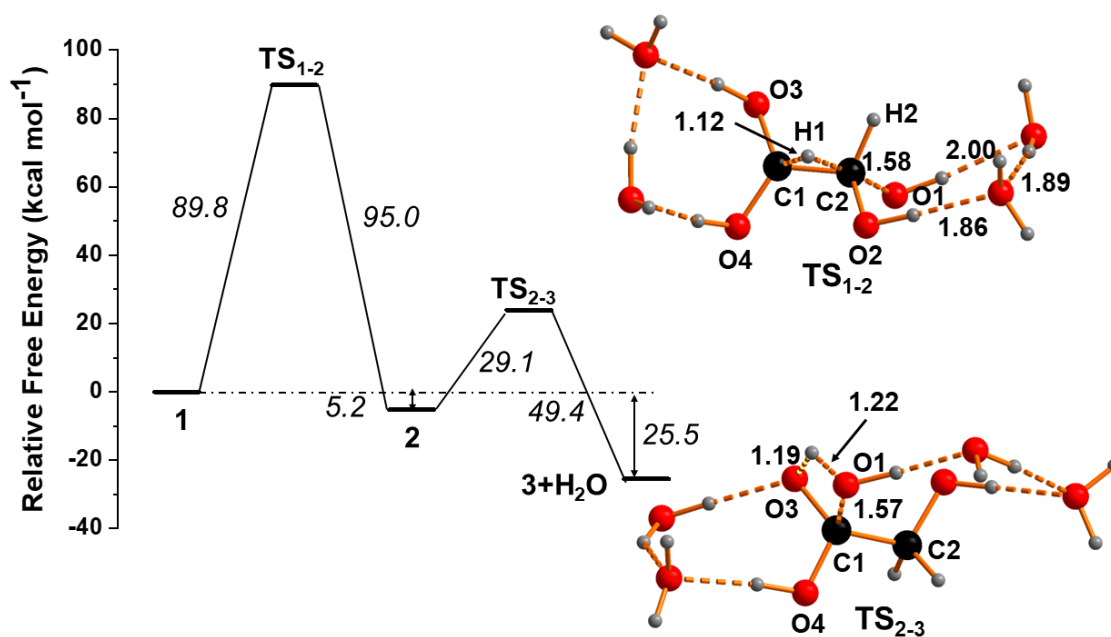


**Figure 4.** Relative Free Energy profile and TS for the non-metal catalyzed conversion of GLY into GA in water under neutral reaction condition.

In order to determine the energy profile for the conversion of **1** under basic reaction condition (Figure 5), the deprotonated form of **1** (**1**<sup>-</sup>) was chosen as starting model compound (Figure S7). The deprotonation of **1** is an exergonic reaction (*i.e.* Free energy gain of 22.2 kcal mol<sup>-1</sup>). The intramolecular 1,2-hydride shift of **1**<sup>-</sup> led directly to the formation of GA, which is in contrast to the result obtained under basic condition, stabilized by four water molecules and a hydroxide ion (**4**<sup>-</sup>, Figure S7). The conversion of **1**<sup>-</sup> to **4**<sup>-</sup> is further characterized by an additional energy gain of 34.7 kcal mol<sup>-1</sup>. Importantly, the TS<sub>1-4<sup>-</sup></sub> was found to be significantly lower (58.3 kcal mol<sup>-1</sup>) (Figure 5) compared to the corresponding TS under neutral reaction condition (89.8 kcal mol<sup>-1</sup>) (Figure 4).

Hence the 1,2-hydride shift of GLY dihydrate under basic reaction condition is somehow more favoured compared to neutral condition (*i.e.* Free energy cost of 88.2 kcal mol<sup>-1</sup> (neutral reaction condition) vs 1.4 kcal mol<sup>-1</sup> (basic reaction condition)). In agreement with results obtained from DFT calculations, an NMR experiment carried out at room temperature with GLY in water in the presence of NaOD showed the instantaneous conversion of GLY into sodium glycolate (*i.e.* <sup>13</sup>C{<sup>1</sup>H} NMR, 62.2 ppm (s) CH<sub>2</sub>; 180.1 (s) COOH), whereas in the absence of base, GLY is stable in water forming dihydrate adducts of different conformations (Figure S8).

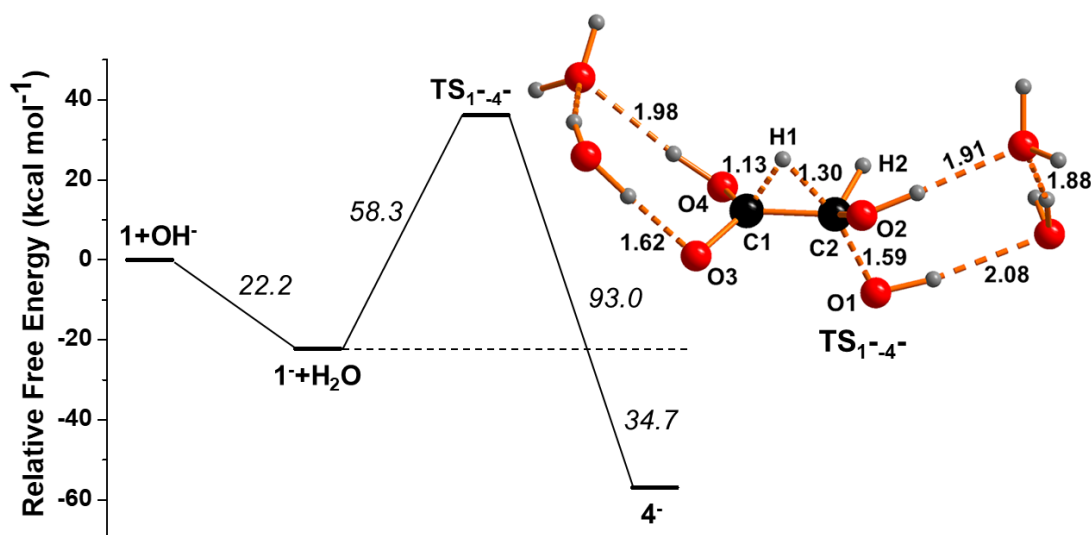


**Figure 5.** Relative Free Energy profile and TS for the non-metal catalyzed conversion of GLY-dihydrate into GA under basic reaction condition.

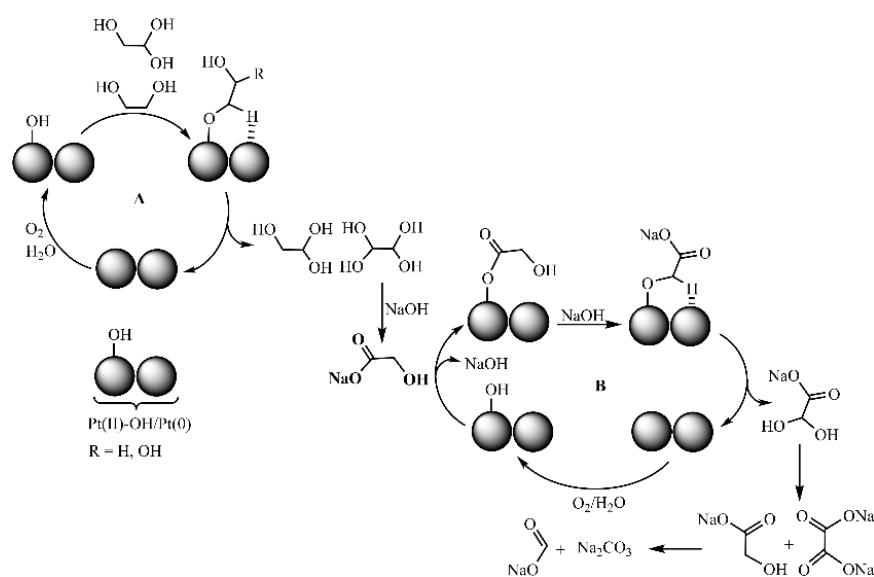
The performance of our best catalyst (Pt<sup>B</sup>@C<sup>K</sup>) under basic reaction condition was compared to that obtained with related Pt-based catalysts under comparable experimental conditions (Table 3). The experimental conditions concerning the molar ratio between EG and Pt vary a lot. In addition, mostly oxygen at high pressure combined with a non-innocent support material was used (Table 3). A comparison of the catalytic performance of carbon supported Pt NPs shows clearly, that Pt<sup>B</sup>@C<sup>K</sup> performs better than a reference system (Table 3, entry 2). Pt onto a non-innocent support material such as ceria brings about strong interaction between the NPs' surface atoms and the support.

Nevertheless, the catalytic activity and GA selectivity is comparable to that obtained with Pt<sup>B</sup>@C<sup>K</sup> (Table 3, entry 3 vs 1). On the other hand, Pt-atoms confined into hydroxyapatite structure leads to a real boost of the catalytic activity (Table 3, entry 4), outperforming Pt NP-based catalysts (Table 3, entry 4 vs 1-3). Unfortunately, only a low EG to Pt molar ratio of 250 was used to test the efficiency of the catalyst.

**Table 3. Comparison of the catalytic activity of heterogeneous Pt-based catalysts used for the aerobic EG oxidation in water under basic reaction condition**

Entry	Catalyst	Reaction condition	EG conv. (%)	GA sel. (%)	TOF (h <sup>-1</sup> )	Reference
1	Pt <sup>B</sup> @C <sup>K</sup>	mol (EG)/mol (Pt) = 7210 T = 140 °C; p(air) = 30 bar	77.4	72.6	3721	This work
2	Pt@C carbon spheres	mol (EG)/mol (Pt) = 1950 T = 70 °C; p(O <sub>2</sub> ) = 10bar	85.2	93	852	19
3	Pt@CeO <sub>2</sub>	mol (EG)/mol (Pt) = 5657 T = 70 °C; p(O <sub>2</sub> ) = 1bar	69	70	3960	21
4	Pt@Hydroxyapatite	mol (EG)/mol (Pt) = 250 T = 50 °C; p(O <sub>2</sub> ) = 10 bar	79	98	6452	31

**Catalytic cycle.** In order to rationalize the increased EG conversion and GA selectivity found in the aerobic EG oxidation carried out under basic condition and in the presence of the best Pt-based catalyst studied herein (Pt<sup>B</sup>@C<sup>K</sup>), we propose the following reaction sequence shown in Scheme 3.



**Scheme 3.** Proposed catalytic cycles operative for the Pt-NP-mediated aerobic oxidation of EG under basic reaction condition.

The proposed catalytic cycles, labelled A and B (Scheme 3) correspond to the reactions which lead to the formation of GA from EG (cycle A) and those which convert GA into undesired reaction products, due to further oxidation (cycle B).

**Ad cycle A:** This cycle comprises the metal NP-catalyzed conversion of EG to the corresponding mono-aldehyde (*i.e.* 2-hydroxy acetaldehyde), which immediately converts by the same reaction mechanism into glyoxal dihydrate (*i.e.* 2-hydroxy-acrtaldehyde has been found in low amounts <1% in the catalytic solutions). The reaction of EG with Pt NPs' surface atoms need the presence of Pt in two different oxidation states (*i.e.* Pt(II) and Pt(0) in close contact to each other). Pt(II) as hydroxide species<sup>41,51,52</sup> (XPS evidence) reacts with EG leading to its activation through the formation of the corresponding Pt-alkoxide species. Upon coordination of the alkoxide to Pt(II) the  $\alpha$ -hydrogen atom is activated<sup>41</sup> and its abstraction occurs through the interaction with the adjacent Pt(0) site. Importantly, the release of 2-hydroxy acetaldehyde or GLY from the NPs' surface occurs along the contemporary reduction of the Pt(II) site to Pt(0) (Scheme 3) and the regeneration of the Pt(II)-OH site occurs by the concomitant presence of molecular oxygen (*i.e.* substitution of air by nitrogen lacks EG conversion (Table 2)) and water as confirmed by theoretical studies.<sup>41,52</sup>

In fact, it has been shown that water plays a dominant role in the dissociation of oxygen upon interaction with mainly the Pt(111) surface metal sites.<sup>41</sup> In addition, the NPs' morphology found for Pt<sup>B</sup>@C<sup>K</sup> (*i.e.* decahedral NPS with the most exposed (111) and 110 facets) fosters the water-mediated surface oxygen activation and the contemporary presence of Pt(II) and Pt(0) (XPS measurements) are prerequisites for a successful EG in GLY conversion. In contrast, Pt<sup>A</sup>@C<sup>K</sup>, which consists of Pt NPs, Pt atoms and small Pt clusters has not the prerequisite for the formation of stable Pt(II)-OH species. Indeed, a strong aggregation of Pt atoms to larger NPs has found to occur in case of Pt<sup>A</sup>@C<sup>K</sup> which contrasts the behaviour of Pt<sup>B</sup>@C<sup>K</sup> under real catalytic condition (*i.e.* PXRD evidence for both recycled catalysts, Figure S6). In addition, XPS analysis conducted on the recycled Pt<sup>B</sup>@C<sup>K</sup> showed a notable increase of the Pt(II) sites on the NP surface compared to the fresh one along with a notable

drop of catalytic EG conversion. An increase of the amount of surface Pt(II) leads to an unfavourable situation on the NPs surface, since not enough Pt(0) sites are in close proximity to Pt(II)-OH which is a prerequisite for the Pt-NP mediated dehydrogenation of the alcohol to the corresponding carbonyl functionality.

GLY-dihydrate, obtained by a double Pt-NP-catalyzed EG dehydrogenation, is a reactive species, particularly in the presence of base (DFT calculations). In fact, the conversion of EG to GA is occurs faster under basic than neutral reaction condition and is not metal-catalyzed as shown by independent catalytic reactions carried out with GLY dihydrate (Table 2).

Ad cycle B: GA is as expected, not inert under the catalytic conditions and reacts under neutral and basic reaction conditions and contemporary presence of the Pt-catalyst to GLYA monohydrate (Scheme 3). The sodium salt of GA coordinates, due to the bifunctionality of GA<sup>53</sup>, mainly by the carboxylate functionality to Pt(II) located at Pt(111).<sup>54</sup> This latter glycolate coordination mode negatively influences the activation of the hydroxy group of GA by surface Pt(II)-OH. The presence of base, shift the equilibrium between carboxylate and alkoxyate coordination of glycolate versus the latter (Scheme 3). In fact, GA conversion increases with increasing base concentration, Table 2, entry 23). As a consequence, glycolate dehydrogenation to glyoxylate occurs upon the same Pt-metal catalyzed reaction sequence as described above for EG and 2-hydroxy-acetaldehyde. In contrast to neutral reaction conditions, the GA dehydrogenation under basic reaction conditions occurs more slowly compared to EG dehydrogenation to GLY, which is clearly confirmed by the corresponding independent catalytic reactions conducted with EG and GA under identical catalytic reactions (Table 2, entry 23 vs 19 and 12 vs 11)

GLYA hydrate converts in water under non-metal catalyzed experimental conditions and absence of base to FA and to a much higher extend to CO<sub>2</sub> (Table 2). The same reaction conducted in the presence of sodium hydroxide leads to sodium glycolate and disodium oxalate (products of an intermolecular Cannizzaro reaction<sup>55</sup>), as proved by an NMR experiment (Figure S9). Hence, upon

this latter reaction, GA is partially recovered and contributes thus to the observed GA selectivity. Disodium oxalate decomposes under the used catalytic reactions to FA and CO<sub>2</sub>.

## CONCLUSIONS

Herein we showed that a carbon supported Pt-based catalyst, generated by the MVS technique using mesitylene as metal solvating agent, was characterized by a variety of Pt morphologies ranging from Pt atom to small Pt-NPs (1.5 nm). Controlled heating (500 °C) of the as-synthesized catalyst in a nitrogen atmosphere gave decahedral NPs (1.5 nm), which proved to be much more active in the aerobic EG oxidation in water under basic condition compared to the as-synthesized catalyst, obtaining a catalytic activity of 3721 h<sup>-1</sup> (surface atom-related TOF,) at an EG conversion and GA selectivity of 77.4 and 72.6%, respectively. The morphology of the heat-treated sample (Pt<sup>B</sup>@C<sup>K</sup>) is fundamental not only for the stability of the catalytically active Pt(II)-OH species but also for the stability against aggregation (i.e. formation of larger NPs), which was significant in case of the as-synthesized catalyst.

Independent catalytic reactions carried out with EG and GA under neutral and basic reaction conditions underscored the importance of the base, not only for the catalytic activity but also the GA selectivity. The GA selectivity is steered by the two catalytic cycles (A and B, Scheme 3) which operate simultaneously. Basic reaction condition favour cycle A (GA formation) compared to cycle B (further oxidation of GA), leading to high GA selectivity, while under neutral reaction condition the opposite is the case.

## EXPERIMENTAL SECTION

**Materials.** EG, GA, GLYA, GLY, OA, sodium hydroxide and  $\text{K}_2\text{PtCl}_6$  (99.9 %) were purchased from Aldrich and used as received. Mesitylene and *n*-pentane were purchased from Aldrich and distilled and stored under argon. Bi-distilled water and compressed air of 5.5 purity was used. Ketjenblack ( $\text{C}^{\text{K}}$ ) was purchased from Cabot Corp. USA and used as received. Compressed synthetic air (5.5) and nitrogen (5.5) were purchased from Rivoira (Italy). **Caution!** *Water solutions of sodium hydroxide at high temperature are highly corrosive. Hence Teflon-coated autoclaves are needed to be used. Since gases at high pressure have been used, the security valve of the autoclave needs to be checked periodically and gases should be released at low temperature (10 °C) in order to avoid losing volatile organic products.*

**Preparation of the catalysts.** The syntheses of the  $\text{C}^{\text{K}}$ -supported Pt catalysts ( $\text{Pt}^{\text{A/B/C}}@C^{\text{K}}$ , Scheme 1) were carried out following a two steps synthesis process: (i) Pt NPs were generated by applying the metal vapor synthesis (MVS) method.<sup>42</sup> To this end, Pt vapor, generated at  $10^{-5}$  mbar by resistive heating of a tungsten wire coated with electrodeposited platinum (ca. 108.0 mg), was condensed with mesitylene vapor (100 mL) onto the cold walls of a glass reactor maintained at -196 °C (liquid nitrogen) for 1 h. The reactor chamber was then heated to the melting point of the solid matrix (ca. -40 °C) and the resulting mesitylene-stabilized Pt solvated metal atoms ( $\text{Pt}^{\text{A}}$ ) solution (96.0 mL, 0.70 mg/mL Pt, measured by ICP) was kept under argon atmosphere in a Schlenk tube at -80 °C. (ii) The generated  $\text{Pt}^{\text{A}}$  solution was added to  $\text{C}^{\text{K}}$  (5.6 g) dispersed in mesitylene (50.0 mL) under stirring, which was continued for 12 h. Afterwards the solvent was removed by vacuum and the obtained solid ( $\text{Pt}^{\text{A}}@C^{\text{K}}$ ) was washed with *n*-pentane (3 x 50 mL) and dried under reduced pressure. The isolated sample was analyzed by ICP-OES showing a Pt content of 1.2 wt%. A portion of  $\text{Pt}^{\text{A}}@C^{\text{K}}$  (0.50 g) was inserted in a tubular quartz oven which was continuously flushed with a flow of nitrogen. The quartz tube was then heated to 500 °C with a heating rate of 15 °C/min and then kept at 500 °C for

half an hour, followed by cooling (under nitrogen) and isolation of the heat-treated powder (Pt<sup>B</sup>@C<sup>K</sup>) at room temperature. Another portion of Pt<sup>A</sup>@C<sup>K</sup> (0.50 g) was heated to the same temperature applying the identical heating rate, but keeping the final temperature for two hours, followed by isolation of the powder at room temperature (Pt<sup>C</sup>@C<sup>K</sup>).

**Characterization of the catalysts.** ICP-OES analyses were carried out with an ICP-Optical emission dual view Perkin Elmer OPTIMA 8000 apparatus. A sample (0.5 mL) of Pt-SMA solution was heated over a heating plate in a porcelain crucible in the presence of aqua regia (2.0 mL) for 6h, dissolving the solid residue in 0.5 M aqueous HCl. The limit of detection (Iod) calculated for platinum was 2 ppb. NMR spectra were recorded at room temperature with a Bruker AVANCE 400 spectrometer (<sup>1</sup>H at 400.0 MHz, <sup>13</sup>C{<sup>1</sup>H} at 101.0 MHz). HAADF-STEM images were acquired on a JEOL ARM200F microscope at the electron Physical Science Imaging Centre (ePSIC) at Diamond Light Source. An acceleration voltage of 200 kV, a convergence semi-angle of 23 mrad and a high-angle annular dark field (HAADF) inner angle of 79 mrad were used for data collection. HAADF-STEM images were also acquired on a JEOL ARM300F microscope (at ePSIC), using an acceleration voltage of 300 kV, a convergence semi-angle of 26.2 mrad and a beam current of 25 pA. An approximate inner collection angle of 92.6 mrad was used to capture HAADF images. A ThermoFisher Spectra 200 (at Cardiff University) was also used to acquire HAADF-STEM images. An accelerating voltage of 200 kV, beam current of 60 pA and a convergence semi-angle of 29.5 mrad were used. HAADF images were acquired with an inner collection angle of a 56 mrad inner angle, and a 200 mrad outer collection angle. A 5–15-minute beam shower was undertaken prior to imaging on any microscope to reduce contamination. Samples for electron microscopy were prepared by their suspension in *iso*-propyl alcohol and ultrasonic dispersion followed by a deposition of a drop of the suspension onto a holey carbon coated grid of either molybdenum, copper or gold (300 mesh). Particle size distribution analysis was completed via the ParticleSpy Python package (reference to <https://zenodo.org/records/5094360>). Otsu filtering was applied for automated particle detection and

measurement, with manual counting verification for single atoms to ensure accuracy. XPS analyses were carried out in a ultra-high vacuum chamber system with a base pressure of  $10^{-9}/10^{-10}$  mbar. The radiation used was a non-monochromatized Al radiation ( $h\nu = 1486.6$  eV, VSW-TA10) combined with a hemispherical electron/ion energy analyser (VSW-HA100 equipped with a 16-channel detector). The operating power of the used Al X-ray source was 120 W (12 kV and 10 mA) and photoelectrons were collected normal to the sample surface, maintaining the analyser angle between the analyser axis and X-ray source fixed at  $54.5^\circ$ . The spectra were acquired in a fixed analyser transmission (FAT) mode (pass energy of 44 eV). The XPS calibration was conducted using 44.0 eV as pass energy. The XPS spectra calibration was conducted by setting the C  $sp^2$  component of the C1s signal to 285.1 eV.<sup>56</sup> All spectra were analyzed using CasaXPS software, and a Shirley function was used to subtract the background. The deconvolution of XPS spectra has been performed by applying a Lorentzian Asymmetry (LA) line-shape. Powder X-ray diffraction (PXRD) spectra were acquired with a PANalytical X'PERT PRO powder diffractometer, using Cu  $K_\alpha$  radiation ( $\lambda = 1.5418$  Å) and a Si wafer (zero background) as sample holder. The spectra were acquired at room temperature in the  $2\theta$  range between  $25$  and  $95^\circ$ , using a step size of  $0.1050^\circ$ . The CO stripping voltammetry experiments were performed in a PAR classical three electrode glass cell, using a KCl-saturated silver-silver chloride reference electrode and a glass-encased platinum wire as counter electrode. The working electrode (PINE, glassy carbon,  $A = 0.1963$  cm<sup>2</sup>) was first polished down to  $0.05$   $\mu\text{m}$  with diamond paste, followed by storing it under stirring alumina ( $0.5$   $\mu\text{m}$ ). Afterwards the catalysts were deposited onto the electrode (glassy carbon) by drop-casting of a catalyst dispersion ( $6.0$   $\mu\text{L}$ ) in a (10:1) mixture of *iso*-propanol and water, followed by drying under a nitrogen atmosphere. The catalyst dispersions used were prepared by ultrasonic bath mixing (1h) of the catalyst (10.0 mg) in *iso*-propanol (1.0 mL) and milliQ water (0.1 mL). After complete drying, a 0.5% nafion solution in 2-propanol ( $2.0$   $\mu\text{L}$ ) was dropcast on top of the catalyst layer to ensure good binding to the glassy carbon substrate. All potentials reported are referenced against the reversible hydrogen electrode (RHE). CO stripping voltammetry experiments were performed as follows: The aqueous solution was saturated

with CO upon bubbling it for 30 min through the solution, followed by applying a potential of 0 V vs Ag | AgCl | KCl<sub>sat</sub> to the working electrode and continuing bubbling for another 30 min. Then, nitrogen was bubbled through the solution of the electrochemical cell followed by scanning the electrode in the potential range between 0 and 1.2 V vs Ag | AgCl | KCl<sub>sat</sub> and applying a scan rate of 50 mV/s for at least two scans to assure the complete desorption of CO. The electrochemically active surface area (ECSA) was determined by integrating the charge and considering a monolayer of linearly-bonded CO (420  $\mu\text{C}/\text{cm}^2$ ).<sup>57</sup>

**DFT calculations.** All the compounds were optimized within Gaussian 16 package,<sup>58</sup> using B97D functional.<sup>59,60</sup> The molecular structures have been validated as minima by frequencies calculations. In all calculations water (*i.e.* reaction medium) was considered within the CPCM model.<sup>61</sup> Triple Zeta basis set<sup>62</sup> was adopted for all the atomic species. The coordinates of all the optimized structures as well as the energetic features are provided as supplementary material.

**Catalytic reactions.** EG (13.70 mmol), water (50.0 mL), catalyst (31.90 mg; Pt, 1.90  $\mu\text{mol}$ ) and NaOH (13.70 mmol) were added to a teflonated stainless steel autoclave (300.0 mL), which was sealed and pressurized with air to 15.0 bar. Afterwards the autoclave was heated to 140 °C by means of an electric heating mantle under continuous mechanical stirring (1000 rpm). Once the latter temperature had been reached, the air pressure was adjusted to 30.0 bar and stirring continued for the desired time. Afterwards, the autoclave was cooled down to 10 °C by means of an ice-water bath and the headspace analyzed by gas chromatography. The catalytic suspension was filtered by means of a paper filter in order to separate the solid catalyst from solution and the latter was then analyzed by HPLC. The headspace of the autoclave was analyzed by means of a Shimadzu 2010 apparatus, using He as carrier gas, a TCD-17 detector and a Carboxen 1010 PLOT fused silica capillary column (30.0 m  $\times$  0.32 mm). The catalytic solutions, recovered after separation from the solid catalyst, were analyzed by a HPLC apparatus (Shimadzu), equipped with an Aminex HPX-87H chromatographic column (300.0 mm  $\times$  7.8 mm) (BIO RAD), and an RID 10A detector. The HPLC analyses parameters

applied were the following: eluent (sulphuric acid, 0.005M) flow rate of 0.4 mL/min, column temperature of 65 °C and injection volume of 10.0 µL (loop). The quantification of the EG conversion and of the organic compounds formed was obtained by means of calibration curves, which were determined for each organic compound. EG conversion, GA selectivity and catalyst activity (TOF) have been defined as follows:

$$\text{EG conversion (\%)} = 100 \times [\text{initial mmol (EG)} - \text{recovered mmol (EG)}] / \text{initial mmol (EG)}$$

$$\text{Selectivity (GA) (\%)} = 100 \times [\text{mmol (GA)} / \text{mmol (EG conv.)}]$$

Catalyst activity expressed in surface atom-related TOF: converted mmol (EG) / [mmol (surface Pt atoms) × h]. The amount of surface atoms in Pt<sup>A/B</sup>@C<sup>K</sup> was calculated by determining the Pt dispersion in each sample (TEM measurements): Pt<sup>A</sup>@C<sup>K</sup>, 73% dispersion (1.39 µmol surface atoms) and Pt<sup>B</sup>@C<sup>K</sup>, 50% dispersion (0.95 µmol surface atoms), whereas for Pt<sup>C</sup>@C<sup>K</sup> the dispersion was not determined due to the inhomogeneity of the sample.

## ASSOCIATED CONTENT

### Supporting Information

The Supporting Information is available free of charge at..

HAADF-STEM images, HPLC-chromatograms, GC-TCD chromatogram, XPS data, <sup>13</sup>C{<sup>1</sup>H} NMR spectra, and atom coordinates of the model compounds used for DFT calculations.

### Notes

The authors declare no competing financial interest.

## ACKNOWLEDGMENTS

The authors thank Mr. Brunetto Cortigiani for his assistance in using the MatchLab (University of Florence) platform. We thank Diamond Light Source for access and support in use of the electron Physical Science Imaging Centre (Instrument E01 and proposal number MG33438) that contributed to the results presented here. Thanks, are also due to Carlo Bartoli (technician at ICCOM-CNR) for the construction of the Teflon-coated autoclave used for catalytic reactions.

## REFERENCES

- (1) Lachaux, C.; Frazao, C. J. R.; Kraußer, F.; Morin, N.; Walther, T.; Francois, L. M. A new Synthetic Pathway for the Bioproduction of Glycolic Acid from Lignocellulosic Sugars Aimed at Maximal Carbon Conservation. *Frontiers in Bioengineering and Biotechnology* **2019**, *7*, 1-12.
- (2) Rosenboom, J.-G.; Langer, R.; Traverso, G. Bioplastics for a circular economy. *Nature Reviews Materials* **2022**, *7*, 117-137.
- (3) Murcia Valderrama, M. A.; van Putten, R.-J.; Gruter, G.-J. M. The Potential of Oxalic and Glycolic Acid-Based Polyesters (Review). Towards CO<sub>2</sub> as a Feedstock (Carbon Capture and Utilization-CCU). *Eur. Polym. J.* **2019**, *119*, 445-468.
- (4) Samantaray, P. K.; Little, A.; Haddelton, D. M.; McNally, T.; Tan, B.; Sun, Z.; Huang, W.; Ji, Y.; Wan, C. Poly (Glycolic Acid) (PGA): A Versatile Building Block Expanding High Performance and Sustainable Bioplastic Applications. *Green Chem.* **2020**, *22*, 4055-4081.
- (5) Gentile, P.; Chiono, V.; Carmagnola, I.; Hatton, P. V. An Overview of Poly(lactic-co-glycolic) Acid (PLGA)-Based Biomaterials for Bone Tissue Engineering. *Int. J. Mol. Sci.* **2014**, *15*, 3640-3659.

- (6) Yunhai, S.; Houyong, S.; Haiyong, C.; Deming, L.; Qinghua, L. Synergistic Extraction of Glycolic Acid from Glycolonitrile Hydrolysate. *Ind. Eng. Chem. Res.* **2011**, *50*, 8216-8224.
- (7) Ebmeyer, F.; Häberlein, H.; Häberlein, H. H.; Häberlein, J. T.; Häberlein, M. C.; Mohn, H.; *Process for Preparing a Particularly Pure Glycolic Acid*. U.S Patent US 5,723, 662, **1998**.
- (8) Drent, E.; Mul, W. P.; Ruisch, B. J. *Process for the Carbonylation of Formaldehyde*. U.S Patent US 6,376,723B2, **2002**.
- (9) Göktürk, E.; Pemba, A. G.; Miller, S. A. Polyglycolic Acid from the Direct Polymerization of Renewable C1 Feedstocks. *Polym. Chem.* **2015**, *6*, 3918-3925.
- (10) Iglesias, J.; Martinez-Salazar, I.; Maireles-Torres, P.; Alonso, D. M.; Mariscal, R.; López Granados, M. Advances in Catalytic Routes for the Production of Carboxylic Acids from Biomass: a Step Forward for Sustainable Polymers. *Chem. Soc. Rev.* **2020**, *49*, 5704-5771.
- (11) Zhang, J.; Liu, X.; Sun, M.; Ma, X.; Han, Y. Direct Conversion of Cellulose to Glycolic Acid with a Phosphomolybdic Acid Catalyst in a Water Medium. *ACS Catal.* **2012**, *2*, 1698-1702.
- (12) Bayu, A.; Karnjanakom, S.; Yoshida, A.; Kusakabe, K.; Abudula, A.; Guan, G.; Polyoxomolybdates Catalysed Cascade Conversions of Cellulose to Glycolic Acid with Molecular Oxygen via Selective Aldohexoses Pathways (an Epimerization and a [2+4] Retro-Aldol Reaction). *Catal. Today* **2019**, *332*, 28-34.
- (13) C. Guarín, C.; Gavilá, L.; Constantí, M.; Medina, F.; Impact of Cellulose Treatment with Hydrotalcites in Hydrothermal Catalytic Conversion. *Chem. Eng. Sci.* **2018**, *179*, 83-91.
- (14) Nazeri, G.; Liaw, S. B.; Yu, Y.; Wu, H. Formation of Organic Acids During Cellobiose Decomposition in Hot-Compressed Water. *Fuel* **2018**, *218*, 174-178.

- (15) Zhou, X.; Zha, M.; Cao, J.; Yan, H.; Feng, X.; Chen, D.; Yang, C. Glycolic Acid Production from Ethylene Glycol via Sustainable Biomass Energy: Integrated Conceptual Process Design and Comparative Techno-Economic-Society-Environment Analysis. *ACS Sustainable Chem. Eng.* **2021**, *9*, 10948-10962.
- (16) Sankar, M.; Dimitratos, N.; Knight, D. W.; Carley, A. F.; Tiruvalam, R.; Kiely, C. J.; Thomas, D.; Hutchings, G. J. Oxidation of Glycerol to Glycolate by Using Supported Gold and Palladium Nanoparticles. *ChemSusChem* **2009**, *2*, 1145-1151.
- (17) Griffin, M. B.; Rodriguez, A. A.; Montemore, M. M.; Monnier, J. R.; Williams, C. T.; Medlin, J. W.; The Selective Oxidation of Ethylene Glycol and 1,2-Propanediol on Au, Pd, and Au-Pd Bimetallic Catalysts. *J. Catal.* **2013**, *307*, 111-120.
- (18) Yan, H.; Yao, S.; Wang, J.; Zhao, S.; Sun, Y.; Liu, M.; Zhou, X.; Zhang, G.; Jin, X.; Feng, X.; Liu, Y.; Chen, X.; Chen, D.; Yang, C. Engineering Pt-Mn<sub>2</sub>O<sub>3</sub> Interface to Boost Selective Oxidation of Ethylene Glycol to Glycolic Acid. *Appl. Catal. B: Env.* **2021**, *284*, 119803.
- (19) Huang, Z.; Li, F.; Chen, B.; Xue, F.; Yuan, Y.; Chen, G.; Yuan, G. Efficient and Recyclable Catalysts for Selective Oxidation of Polyols in H<sub>2</sub>O with Molecular Oxygen. *Green Chem.* **2011**, *13*, 3414-3422.
- (20) Zhan, Y.; Hou, W.; Li, G.; Shen, Y.; Zhang, Y.; Tang, Y. Oxidant-Free Transformation of Ethylene Glycol Toward Glycolic acid in Water. *ACS Sustainable Chem. Eng.* **2019**, *7*, 17559-17564.
- (21) Shi, H.; Yin, X.; Subramaniam, B.; Chaudhari, R. V.; Liquid-Phase Oxidation of Ethylene Glycol on Pt and Pt-Fe Catalysts for the Production of Glycolic Acid: Remarkable Bimetallic Effect and Reaction Mechanism. *Ind. Eng. Chem. Res.* **2019**, *58*, 18561-18568.

- (22) Dapsens, P. Y.; Mondelli, C.; Kusema, B. T.; Verel, R.; Pérez-Ramírez, J. A Continuous Process for Glyoxal Valorisation Using Tailored Lewis-Acid Zeolite Catalysts. *Green Chem.* **2014**, *16*, 1176-1186.
- (23) Schuler, E.; Grooten, L.; Kasireddy, M.; More, S.; Shiju, N. R.; Tanielyan, S. K.; Augustine, R. L.; Gruter, G.-J. M. Oxalic Acid Hydrogenation to Glycolic Acid: Heterogeneous Catalysts Screening. *Green Chem.* **2023**, *25*, 2409-2426.
- (24) Molder, T. D. J.; Kersten, S. R. A.; Lange, J.-P.; Ruiz, M. P. From Woody Biomass to Ethylene Glycol: Inorganics Removal Boosts the Yield. *Ind. Eng. Chem. Res.* **2021**, *60*, 13515-13522.
- (25) Yang, Q.; Fan, Y.; Zhou, J.; Zhao, L. Optimal Integration Design of Sustainable Ethylene Glycol Production Process Considering Economic Benefit and Environmental Impact. *J. Clean. Prod.* **2023**, *396*, 136540.
- (26) Yang, X.; Li, Z.; Guo, M.; Zhao, T.; X. Su, X.; W. Jiang, W.; Han, G.; Ben, H. Synergistic Effects of WO<sub>3</sub> and NiCu Bimetals for the One-Pot Conversion of Cellulose into Ethylene Glycol. *Fuel* **2023**, *341*, 127560.
- (27) Weng, Y.; Wang, Y.; Zhang, M.; Wang, X.; Sun, Q.; Mu, S.; Wang, H.; Fan, M.; Zhang, Y. Selective Chemo-Catalytic Hydrogenolysis of Cellulose to EG and EtOH Over Porous SiO<sub>2</sub> Supported Tungsten Catalysts. *Catal. Today* **2023**, *407*, 89-95.
- (28) Zheng, M.-Y.; Wang, A.-Q.; Ji, N.; Pang, J.-F.; Wang, X.-D.; Zhang, T. Transition Metal-Tungsten Bimetallic Catalysts for the Conversion of Cellulose into Ethylene Glycol. *ChemSusChem* **2010**, *3*, 63-66.
- (29) Wang, A.; Zhang, T.; One-Pot Conversion of Cellulose to Ethylene Glycol with Multifunctional Tungsten-Based Catalysts. *Acc. Chem. Res.* **2013**, *46*, 1377-1386.

- (30) Yan, H.; Zhao, M.; Cao, Y.; Zhou, X.; Liu, Y.; Chen, X.; Feng, X.; Duan, X.; Zaera, F.; Zhou, X.; Yang, C. Crystal-Facet-Dependent, Electron Sink Effect for the Enhanced Selective Oxidation of Polyols at the Secondary Hydroxyl Position. *J. Catal.* **2024**, *431*, 115401.
- (31) Yan, H.; Zhao, M.; Feng, X.; Zhao, S.; Zhou, X.; Li, S.; Zha, M.; Meng, F.; Chen, X.; Liu, Y.; Chen, D.; Yan, N.; Yang, C.  $\text{PO}_4^{3-}$  Coordinated Robust Single-Atom Platinum Catalyst for Selective Polyol Oxidation. *Angew. Chem. Int. Ed.* **2022**, *61*, e202116059.
- (32) Kuwauchi, Y.; Yoshida, H.; Akita, T.; Haruta, M.; Takeda, S. Intrinsic Catalytic Structure of Gold Nanoparticles Supported on  $\text{TiO}_2$ . *Angew. Chem. Int. Ed.* **2012**, *51*, 7729-7733.
- (33) Frey, H.; Beck, A.; Huang, X.; van Bokhoven, J. A.; Willinger, M. G. Dynamic Interplay Between Metal Nanoparticles and Oxide Support under Redox Conditions. *Science* **2022**, *376*, 982-987.
- (34) Yuan, W.; Zhu, B.; Fang, K.; Li, X.-Y.; Hansan, T. W.; Ou, Y.; Yang, H.; Wagner, J. B.; Gao, Y.; Wang, Y.; Zhang, Z. In Situ Manipulation of the Active Au- $\text{TiO}_2$  Interface with Atomic Precision During CO Oxidation. *Science* **2021**, *371*, 517-521.
- (35) Zhang, S.; Plessow, P. N.; Willis, J. J.; Dai, S.; Xu, M.; Graham, G. W.; Cargnello, M.; Abild-Pedersen, F.; Pan, X. Dynamic Observation and Detailed Description of Catalysts Under Strong Metal-Support Interaction. *Nano Lett.* **2016**, *16*, 4528-4534.
- (36) Chung, D. Y.; Chung, Y.-H.; Jung, N.; Choi, K.-H.; Sung, Y.-E. Correlation Between Platinum Nanoparticle Surface Rearrangement Induced by Heat Treatment and Activity for an Oxygen Reduction Reaction. *Phys. Chem. Chem. Phys.* **2013**, *15*, 13658-13663.
- (37) Han, K. S.; Moon, Y.-S.; Han, O. H.; Hwang, K. J.; Kim, I.; Kim, H. Heat Treatment and Potential Cycling Effects on Surface Morphology, Particle Size, and Catalytic Activity of Pt/C Catalysts Studied by  $^{13}\text{C}$  NMR, TEM, XRD and CV. *Electrochem. Commun.* **2007**, *9*, 317-324.

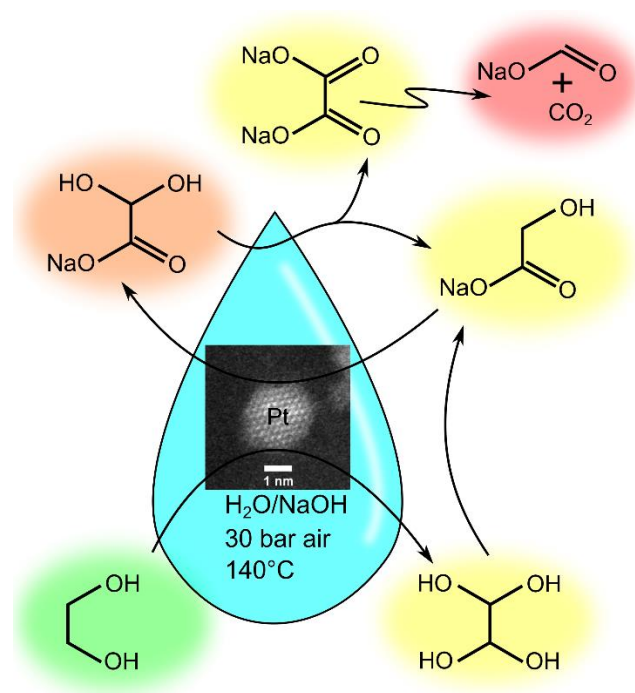
- (38) Bezerra, C. W. B.; Zhang, L.; Liu, H.; Lee, K.; Marques, A. L. B.; Marques, E. P.; Wang, H.; Zhang, J. A Review of Heat-Treatment Effects on Activity and Stability of PEM Fuel Cell Catalysts for Oxygen Reduction Reaction. *Power Sources* **2007**, *173*, 891-908.
- (39) Vara, M.; Wang, X.; Howe, J.; Chi, M.; Y. Xia, Y. Understanding the Stability of Pt-Based Nanocages Under Thermal Stress Using *in situ* Electron Microscopy. *ChemNanoMat* **2018**, *4*, 112-117.
- (40) Gilroy, K. D.; Elnabawy, A. O.; Yang, T.-H.; Roling, L. T.; Howe, J.; Mavrikakis, M.; Xia, Y. Thermal Stability of Metal Nanocrystals: An Investigation of the Surface and Bulk Reconstructions of Pd Concave Icosahedra. *Nano Lett.* **2017**, *17*, 3655-3661.
- (41) Yan, H.; Yao, S.; Liang, W.; Feng, X.; Jin X.; Liu, Y.; Chen, X.; Yang, C. Selective Oxidation of Glycerol to Carboxylic Acid on Pt(111) in Base-Free Medium: A Periodic Density Functional Theory Investigation. *Appl. Surf. Sci.* **2019**, *497*, 143661.
- (42) Pitzalis, E.; Psaro, R.; Evangelisti, C. From Metal Vapor to Supported Single Atoms, Clusters and Nanoparticles: Recent Advances to Heterogeneous Catalysts. *Inorg. Chim. Acta* **2022**, *533*, 120782.
- (43) Borodziński, A.; Bonarowska, M. Relation Between Crystallite Size and Dispersion on Supported Metal Catalysts. *Langmuir* **1997**, *13*, 5613-5620.
- (44) Long, N. V.; Ohtaki, M.; Uchida, M.; Jalem, R.; Hirata, H.; Chien, N. D.; Nogami, M. Synthesis and Characterization of Polyhedral Pt Nanoparticles: Their Catalytic Property, Surface Attachment, Self-Aggregation and Assembly. *J. Colloid and Int. Sci.* **2011**, *359*, 339-350.
- (45) Maillard, F.; Schreier, S.; Hanzlik, M.; Savinova, E. R.; Weinkauff, S.; Stimming, U. Influence of Particle Agglomeration on the Catalytic Activity of Carbon-Supported Pt Nanoparticles in CO Monolayer Oxidation. *Phys. Chem. Chem. Phys.* **2005**, *7*, 385-393.

- (46) Maillard, F.; Savinova, E.R.; Simonov, P. A.; Zaikovskii, V. I.; Stimming, U. Infrared Spectroscopic Study of CO Adsorption and Electro-Oxidation on Carbon-Supported Pt Nanoparticles: Interparticle versus Intraparticle Heterogeneity. *J. Phys. Chem. B* **2004**, *108*, 17893-17904.
- (47) Ciapina, E. G.; Santos, S. F.; Gonzalez, E. R. Electrochemical CO Stripping on Nanosized Pt Surfaces in Acid Media: A Review on the Issue of Peak Multiplicity. *J. Electroanal. Chem.* **2018**, *815*, 47-60.
- (48) Ono, L. K.; Yuan, B.; Heinrich, H.; Cuenya, B. R. Formation and Thermal Stability of Platinum Oxides on Size-Selected Platinum Nanoparticles: Support effects. *J. Phys. Chem. C* **2010**, *114*, 22119-22133.
- (49) Yohannes, A. G.; Fink, K.; Kondov, I. Pt Nanoparticles under Oxidizing Conditions- Implications of Particle Size, Adsorption Sites and Oxygen Coverage on Stability. *Nanoscale Adv.* **2022**, *4*, 4554-4569.
- (50) Ohshima, T.; Yamamoto, Y.; Takaki, U.; Inoue, Y.; Saeki, T.; Itou, K.; Maegawa, Y.; Iwasaki, T.; Mashima, K. Theoretical Study of Al(III)-Catalyzed Conversion of Glyoxal to Glycolic acid: Dual Activated 1,2-Hydride Shift Mechanism by Protonated Al(OH)<sub>3</sub> Species. *Chem. Commun.* **2009**, 2688-2690.
- (51) Mom, R. V.; Knop-Gericke, A. Hydroxylation of Platinum Surface Oxides Induced by Water Vapor. *J. Phys. Chem. Lett.* **2022**, *13*, 879-883.
- (52) Zope, B. N.; Hibbitts, D. D.; Neurock, M.; Davis, R. J. Reactivity of the Gold/Water Interface During Selective Oxidation Catalysis. *Science* **2010**, *330*, 74-78.
- (53) Bermejo, E.; Carballo, R.; Castiñeiras, A.; Lago, A. B. Coordination of  $\alpha$ -Hydroxycarboxylic Acids with First-Row Transition Ions. *Coord. Chem. Rev.* **2013**, *257*, 2639-2651.

- (54) Delgado, J. M.; Blanco, R.; Orts, J. M.; Perez, J. M.; Rodes, A. Glycolate Adsorption at Gold and Platinum Electrodes: A Theoretical and in Situ Spectroscopic Study. *Electrochim. Acta* **2010**, *55*, 2055-2064.
- (55) Wang, P.; Tao, W.-J.; Sun, X.-L.; Liao, S.; Tang, Y. A Highly Efficient and Enantioselective Intramolecular Cannizzaro Reaction Under TOX/Cu(II) Catalysis. *J. Am. Chem. Soc.* **2013**, *135*, 16849-16852.
- (56) Vovk, E. I.; Kalinkin, A. V.; Smirnov, M. Y.; Klembovskii, I. O.; Bukhtiyarov, V. I. XPS Study of Stability and Reactivity of Oxidized Pt Nanoparticles Supported on TiO<sub>2</sub>. *J. Phys. Chem. C* **2017**, *121*, 17297-17304.
- (57) Binninger, T.; Fabbri, E.; Kötzt, R.; Schmidt, T. Determination of the Electrochemically Active Surface Area of Metal-Oxide Supported Platinum Catalyst. *J. Electrochem. Soc.* **2014**, *161*, H121-H128.
- (58) Frisch, M. J.; Trucks, G. W.; Schlegel, H. B.; Scuseria, G. E.; Robb, M. A.; Cheeseman, J. R.; Scalmani, G.; Barone, V.; Petersson, G. A.; Nakatsuji, H.; Li, X.; Caricato, M.; Marenich, A. V.; Bloino, J.; Janesko, B. G.; Gomperts, R.; Mennucci, B.; Hratchian, H. P.; Ortiz, J. V.; Izmaylov, A. F.; Sonnenberg, J. L.; Williams-Young, D.; Ding, F.; Lipparini, F.; Egidi, F.; Goings, J.; Peng, B.; Petrone, A.; Henderson, T.; Ranasinghe, D.; Zakrzewski, V. G.; Gao, J.; Rega, N.; Zheng, G.; Liang, W.; Hada, M.; Ehara, M.; Toyota, K.; Fukuda, R.; Hasegawa, J.; Ishida, M.; Nakajima, T.; Honda, Y.; Kitao, O.; Nakai, H.; Vreven, T.; Throssell, K.; Montgomery, J. A. Jr.; Peralta, J. E.; Ogliaro, F.; Bearpark, M. J.; Heyd, J. J.; Brothers, E. N.; Kudin, K. N.; Staroverov, V. N.; Keith, T. A.; Kobayashi, R.; Normand, J.; Raghavachari, K.; Rendell, A. P.; Burant, J. C.; Iyengar, S. S.; Tomasi, J.; Cossi, M.; Millam, J. M.; Klene, M.; Adamo, C.; Cammi, R.; Ochterski, J. W.; Martin, R. L.; Morokuma, K.; Farkas, O.; Foresman, J. B.; Fox, D. J. *Gaussian 16, revision C.01; Gaussian, Inc.: Wallingford, CT, 2016*.

- (59) Becke, A. D. Density-Functional Thermochemistry. V. Systematic Optimization of Exchange-Correlation Functionals. *J. Chem. Phys.* **1997**, *107*, 8554-8560.
- (60) Grimme, S. Semiempirical GGA-type Density Functional Constructed With a Long-Range Dispersion Correction. *J. Comput. Chem.* **2006**, *27*, 1787-1799
- (61) Barone, V.; Cossi, M. Quantum Calculation of Molecular Energies and Energy Gradients in Solution by a Conductor Solvent Model. *J. Chem. Phys. A* **1998**, *102*, 1995-2001.
- (62) Schäfer, A.; Huber, C.; Ahlrichs, R. Fully-Optimized Contracted Gaussian Basis Sets of Triple Zeta Valence Quality for Atoms Li to Kr. *J. Chem. Phys.* **1994**, *100*, 5829-5835.

## Graphical Abstract



Heat treatment of carbon supported platinum nanoparticles, solvated by mesitylene (metal vapour synthesis), brought about the formation of dodecahedral nanoparticles, which proved to be highly active in the aerobic oxidation of ethylene glycol to glycolic acid in water under basic reaction condition.